Atmos. Chem. Phys. Discuss., 14, 20231–20257, 2014
www.atmos-chem-phys-discuss.net/14/20231/2014/
doi:10.5194/acpd-14-20231-2014

Atmospheric Chemistry and Physics Discussions
Open Access

Analysis of the ozone profile specifications in the WRF-ARW model and their impact on the simulation of direct solar radiation

A. Montornès[1,2], B. Codina[1], and J. W. Zack[3]

[1]Department of Astronomy and Meteorology, University of Barcelona, Barcelona, Spain
[2]Information Services, AWS Truepower, Barcelona, Spain
[3]MESO Inc., Troy, USA

Received: 21 February 2014 – Accepted: 18 July 2014 – Published: 6 August 2014

Correspondence to: A. Montornès (amontornes@am.ub.es)

Published by Copernicus Publications on behalf of the European Geosciences Union.

Abstract

Although ozone is an atmospheric gas with high spatial and temporal variability, mesoscale numerical weather prediction (NWP) models simplify the specification of ozone concentrations used in their shortwave schemes by using a few ozone profiles. In this paper, a two-part study is presented: (i) an assessment of the quality of the ozone profiles provided for use with the shortwave schemes in the Advanced Research version of the Weather Research and Forecasting (WRF-ARW) model and (ii) the impact of deficiencies in those profiles on the performance of model simulations of direct solar radiation. The first part compares simplified datasets used to specify the total ozone column in five schemes (i.e. Goddard, New Goddard, RRTMG, CAM and Fu–Liou–Gu) with the Multi-Sensor Reanalysis dataset during the period 1979–2008 examining the latitudinal, longitudinal and seasonal limitations in the ozone modeling of each parameterization. The results indicate that the maximum deviations are over the poles due to the Brewer–Dobson circulation and there are prominent longitudinal patterns in the departures due to quasi-stationary features forced by the land–sea distribution. In the second part, the bias in the simulated direct solar radiation due to these deviations from the simplified spatial and temporal representation of the ozone distribution is analyzed for the New Goddard and CAM schemes using the Beer–Lambert–Bouger law. For radiative applications those simplifications introduce spatial and temporal biases with near-zero departures over the tropics during all the year and increasing poleward with a maximum in the high middle latitudes during the winter of each hemisphere.

1 Introduction

The shortwave radiation absorption by the surface and the atmosphere is the basic engine that starts the atmospheric system. In a cloudless and clear (i.e. without aerosols) sky, the most important absorbers of the solar radiation in the Earth's atmosphere are water vapor and ozone. Water vapor absorption occurs mainly in the troposphere

ACPD

14, 20231–20257, 2014

because water sources are located on the surface. In contrast, ozone absorbs the shortwave radiation in the stratosphere becoming the major source of heating in that layer (Ramanathan and Dickinson, 1979). In a dynamic frame, the ozone profile should be well detailed in numerical weather prediction (NWP) models which include vertical levels above ~ 50 hPa.

From the point of view of the radiative transfer, the optical properties of the atmosphere (i.e. optical thickness, single scattering albedo, asymmetry factor and backscattering) are defined as a function of the atmospheric composition (i.e. gas species, aerosols, water drops or ice particles among others). Thus, the vertical characterization for the entire atmosphere arises as a critical point. For example the absorption due to the ozone in the stratosphere determines the radiative input energy in the troposphere.

The impact of the ozone variations on the shortwave radiation forecasts from mesoscale NWP models has historically not been treated as a significant issue. This is because, on the one hand, these models are not oriented to stratosphere simulations because the typical timescales in the mesoscale differ from the timescales of the interaction between the stratosphere and the troposphere. Therefore, shortwave schemes in mesoscale NWP models simplify the ozone information reducing the computational resources of this kind of parameterization. These simplifications includes zonal averages and latitudinal, vertical and seasonal discretization that vary between shortwave parameterizations. On the other hand, new applications of the mesoscale NWP models such as the solar energy modeling, require an accurate treatment of the radiative transfer equation throughout the entire atmosphere.

The real ozone mixing ratio shows a high spatial and temporal variability occurring mainly in the stratosphere defining a region denoted by ozone layer as reported in many studies such as in Chipperfield and Jones (1999) or, recently, in Parrondo et al. (2014) among others. Ozone is continuously created and destroyed by photochemical processes associated with solar ultraviolet (UV) radiation. These processes result in an ozone source in the tropics and a net poleward transport, which is referred to as

ACPD
14, 20231–20257, 2014

the Brewer–Dobson circulation (Brewer, 1949; Dobson, 1956). These results in a maximum in the total ozone during the polar night.

This paper presents an analysis of the strategies that are employed to specify the ozone profiles used as input into the shortwave radiation schemes in the WRF-ARW model. The analysis is split into two parts: (i) a study of the simplifications assumed in the ozone profiles and (ii) an analysis of the uncertainties added to the computation of the direct solar radiation.

In the first part, spatial and temporal deviations over the total ozone column are discussed. Each ozone profile provided with the WRF-ARW package is vertically integrated and compared with monthly averaged values from the Multi-Sensor Reanalysis (MSR) dataset (van der A et al., 2010) during the climate period 1979–2008. Surface conditions for the vertical integration are based on the ERA-Interim[1] (Dee et al., 2011) reanalysis for the same climate period.

In the second part, the effect of this error over the direct solar radiation at the surface is computed considering an atmosphere composed only by ozone. The analysis is centered in two shortwave schemes: the New Goddard (Chou and Suarez, 1999; Chou et al., 2001) and the CAM (Collins et al., 2004). Both show the ozone mass absorption coefficient independent of the temperature and the pressure and consequently, the Beer–Lambert–Bouger law may be computed as a function of the total ozone column calculated in the first part.

---

[1]ECMWF ERA-Interim data used in this study have been obtained from the ECMWF data server.

ACPD
14, 20231–20257, 2014

2 Methodology

2.1 Ozone absorption in the WRF-ARW model

The version 3.5 of the WRF-ARW model, available since 2013, includes seven shortwave schemes: Dudhia (available since 2000), Goddard (2000), New Goddard (2011), GFDL (2004), RRTMG (2009), CAM (2006) and FLG (2011).

The Dudhia scheme (Dudhia, 1989) is the simplest shortwave parameterization in the model without any consideration about the ozone absorption. For this reason, this parameterization is not considered in the following analyses.

The Goddard and the New Goddard schemes (Chou and Suarez, 1999; Chou et al., 2001) are similar because the second is an update of the first. The ozone treatment is common for both schemes and is based on Chou and Suarez (1999). From now, both schemes will be denoted as G-NG. In these schemes the solar spectrum is divided into eleven spectral bands (seven in the ultraviolet, UV, one in the visible or photosynthetic active region, PAR, and three in the near-infrared, near-IR). In the UV+PAR spectral regions, G-NG neglect the pressure and temperature (i.e. height) effects over the ozone absorption assuming a constant absorption coefficient in each spectral interval. These coefficients are obtained dividing each band into 127 narrow sub-bands with a width of $\sim 0.003\,\mu m$ and using the ozone absorption coefficient given in WMO (1986). The absorption in the near-IR is added by enhancing the absorption in the PAR region, reducing the computational time. The New Goddard scheme introduces a small correction for the ozone absorption coefficient in the PAR region, from 0.0539 (cm-atm) stp^{-1} to 0.0572 (cm-atm) stp^{-1}. The effect of this correction can be neglected for the purposes of this paper considering both schemes as one. All results are based on New Goddard values since it is the newest version.

The CAM scheme (Collins et al., 2004) splits the spectrum into nineteen bands (seven for the ozone, one in the visible or PAR, seven for the water vapor, three for the carbon dioxide and one for the near-IR). The ozone absorption is computed over the seven ozone bands and over the PAR region as well. As in the previous scheme, the CAM parameterization assumes a constant ozone absorption coefficient for each band. The procedure to compute these coefficients is described in Briegleb (1992).

The GFDL scheme (Lacis and Hansen, 1974) divides the spectrum in two spectral bands: one in the UV+PAR and the other in the near-IR (composed by different subdivisions). The ozone absorption occurs over the UV+PAR region following the parametric formulas described in Lacis and Hansen (1974). Since it is the oldest scheme (i.e. it was implemented in the Eta/NMM model) and the source code implementation differs from the general nomenclature in the WRF-ARW model, this parameterization is avoided in the paper.

The RRTMG (Mlawer et al., 1997) parameterization divides the shortwave spectrum into fourteen bands covering the UV, PAR and near-IR regions and at the same time each spectral band is divided into 16 intervals used to apply the correlated-k distribution method (Liou, 1980). This scheme takes into account the ozone absorption coefficient dependence on pressure and temperature for each spectral band and interval. These values are stored in an external file called RRTMG_SW_DATA.

The Fu–Liou–Gu scheme (Gu et al., 2011) splits the solar spectrum into six spectral bands. As in the RRTMG parameterization, the interaction with the absorber gases is based on the correlated-k distribution method.

Each aforementioned shortwave scheme has available different datasets reproducing ozone mixing ratio conditions in the atmosphere as a function of the pressure (i.e. vertical profile), the latitude and the season. The complexity of these datasets varies from one scheme to the other as it is summarized in Table 1. When a shortwave scheme is called by the model, the profiles are selected and interpolated into the sigma levels defined in the simulation domain.

G-NG and FLG schemes include five ozone profiles based on the same datasets. These profiles simulate the ozone data for Tropical, Mid-latitude (summer/winter) and Arctic (summer/winter) atmospheres. Thresholds to choose one profile or other are based on the latitude of the center of the domain as well as on the day of the year. Tropical regions are assumed between 30° S and 30° N without seasonal variation.

Mid-latitudes and Arctic regions are defined between 30–60 and 60–90°, respectively, considering winter and summer variations. In the Northern Hemisphere, winter is assumed between the 285th and the 80th days of the year and summer between the 81th and the 284th day of the year. In the Southern Hemisphere these thresholds are inverted. The highest level for all these profiles is located at 0.0006244 hPa while surface conditions depend on the location and the season. In the first part, they are referred as G-NG-FLG.

The GFDL parameterization includes latitudinal and time variations with resolutions of 5° and four seasons (winter, spring, summer and fall), respectively. Profiles are composed by 37 vertical levels.

The RRTMG scheme includes two ozone profiles as a function of the season (winter or summer). Nevertheless, this granularity is useless due to the fact that the final used profile is computed as a composition of both, without considering the day of the year. Therefore, only one profile is considered for any latitude and season. The highest level is located at 0.647 hPa. Since version 3.5, this scheme can utilize the ozone profiles available in the CAM scheme with the option o3input in the namelist.input file.

Finally, the CAM scheme includes several ozone profiles loaded from a binary auxiliary file called ozone_formatted with the ozone data and another two named ozone_lat.formatted and ozone_plev.formatted including latitude and pressure values, respectively. This dataset cover 64 latitudes with a resolution ~ 2.28° and 59 pressure levels from 1003 to 0.28 hPa for each month of the year. Ozone values are latitudinally interpolated for each node of the domain.

2.2 Part one: study of the simplifications assumed in the ozone profiles

In this part, ozone profiles of each shortwave parameterization are vertically integrated. Next, they are assigned over a 1° per 1° global domain for each month of a typical year. Then, these values are compared with the baseline typical year.

First, let us assume one shortwave scheme. Given a vertical profile for the ozone mixing ratio called $q_{O_3}(z)$, the total ozone column TO_3, from the ground to the top of

Discussion Paper | Discussion Paper | Discussion Paper | Discussion Paper |

ACPD

14, 20231–20257, 2014

Analysis of the ozone profile specifications in the WRF-ARW model

A. Montornès et al.

the atmosphere (TOA), is defined as

$$TO_3 = \int_0^{\infty} \rho q_{O_3} \mathrm{d}z, \tag{1}$$

where ρ is the dry air density and z is the height respect to the ground.

Under the assumption of a well-stratified atmosphere, the pressure and the geometric height are related by the hydrostatic equation given by

$$\mathrm{d}p = -\rho g \mathrm{d}z, \tag{2}$$

where g is the gravity acceleration, assumed as a constant value.

The hydrostatic equilibrium given by Eq. (2) leads Eq. (1) to

$$TO_3 = \frac{1}{g} \int_0^{p_s} q_{O_3}(p) \mathrm{d}p. \tag{3}$$

where pressure at TOA is zero by definition and the surface pressure is denoted by p_s.

Note that the integration covers the entire atmosphere including the upper levels (i.e. above 86 km) where the diffusion and the vertical transport of the individual gas species loss progressively the hydrostatic equilibrium leading to the need of a dynamically oriented model including the diffuse separation as shown in NOAA (1976). Notwithstanding, the dry air density and the ozone mixing ratio in those layers have an order of magnitude of 10^{-6} kg m^{-3} and 10^{-6} kg kg^{-1}, respectively, and monotonically decreasing. Hence, non-hydrostatic effects may be neglected for the purposes of the current analysis.

Because of available ozone profiles in the shortwave schemes are not analytic functions, Eq. (3) in practice must be solved using a numerical integration scheme such as

Simpson's method. Further, for an ozone profile composed by N vertical levels, Eq. (3) may be discretized such as

$$TO_3 = \frac{1}{6g}\sum_{k=1}^{N-1}(p_k - p_{k+1})(q_{O_3,k} + 0.5(q_{O_3,k} + q_{O_3,k+1}) + q_{O_3,k+1}), \tag{4}$$

where $q_{O_3,k}$ and p_k are the ozone mixing ratio and the pressure at a level k.

This vertical integration requires two boundary conditions: the ozone mixing ratio at the TOA and the pressure at surface. The first one is assumed as zero (i.e. without ozone between the last available level and the TOA). The pressure at surface requires a complex treatment since it shows a dependence on the location and the season. This boundary is computed using the ERA-Interim reanalysis covering the climate period since 1979 until 2008 (i.e. thirty years). This period is not arbitrary since it has been consistent with the baseline data described below. Based on this period, monthly surface pressure averages are computed and used as surface conditions for the vertical integration of the ozone profiles.

From this procedure, the total ozone column for any location of the world and season can be computed. To discuss about the geographical distribution of the errors, a global 1° per 1° grid is built using the latitudinal thresholds fixed in each shortwave scheme as described in Sect. 2.1. For the discussion about the seasonal variability, values are computed throughout the twelve months of a year. Ozone profiles in some shortwave schemes like the New Goddard or the FLG are defined as a function of the day of the year instead of the month. In this situations, months are summarized by the 15th day of the month. This means that January is the 15th day of the year, February is the 46th day of the year, etc.

These gridded results are compared with real data. The data used as a baseline derive from the Multi-sensor reanalysis, MSR (van der A et al., 2010) during the period 1979–2008 and are monthly averaged (this dataset is provided with a monthly resolution).

The MSR was created from all available ozone column data measured by fourteen polar orbiting satellites in the near-ultraviolet Huggins band since November 1978 to December 2008, including TOMS (on the satellites Nimbus-7 and Earth Probe), SBUV (Nimbus-7, NOAA-9, NOAA-11 and NOAA-16), GOME (ERS-2), SCIAMACHY (Envisat), OMI (EOS-Aura), and GOME-2 (Metop-A). The dataset processing includes two steps. In the first one, a bias correction scheme is applied over all satellite observations based on independent ground-based total ozone data from the World Ozone and Ultraviolet Data Center. In the second step, a data assimilation process is applied using a sub-optimal implementation of the Kalman filter method and based on a chemical transport model driven by ECMWF meteorological fields. This dataset shows a bias departure less than 1 % with a root mean square standard deviation of around 2 % as compared to the corrected satellite observations used.

Therefore, for each node i (west–east direction) and j (south–north direction) and, month m, we have two datasets: one for each model under consideration, $TO_{3,\mathrm{sch},ij}(m)$, and the other one describing the baseline data, $TO_{3,\mathrm{MSR},ij}(m)$. Both datasets may be compared node by node for the entire typical year leading a quantification about the error. Hence, the relative error of the parameterization $\epsilon_{ij}(m)$ may be expressed by

$$\epsilon_{ij}(m) = \frac{TO_{3,\mathrm{sch},ij}(m) - TO_{3,\mathrm{MSR},ij}(m)}{TO_{3,\mathrm{MSR},ij}(m)}. \tag{5}$$

This metric will be used to discuss the simplifications assumed within the ozone column by the shortwave schemes.

2.3 Part two: an analysis of the uncertainties added to thecomputation of the direct solar radiation

In the second part of the study, the previous computed total ozone columns are used to examine the ozone absorption over the direct solar radiation and to determine the introduced bias based on climate patterns.

Considering a direct light beam from the Sun, traveling throughout a non-scattering isotropic plane-parallel atmosphere, the monochromatic downward solar flux density, covering the spectral interval $\Delta\lambda$, may we written as

$$F^{\downarrow}_{\lambda,\mathrm{dir}}(\tau_\lambda) = \mu_0 F_0(\lambda) e^{-\tau_\lambda/\mu_0}, \tag{6}$$

where τ_λ is denoted as the optical thickness for the spectral band λ and μ_0 is the cosine of the solar zenith angle. The derivation of Eq. (6) is thoroughly discussed by many literature such as Chandrasekhar (1960) or Liou (1980). This expression is commonly denoted as the Beer–Lambert–Bouguer law.

As described in Liou (1980), due to the structure of the absorption lines, it is required to define the monochromatic absorptance covering the interval $\Delta\lambda$ as

$$A_{\bar{\lambda}}(\tau/\mu_0) = \int_{\Delta\lambda} (1 - e^{-\tau_\lambda/\mu_0}) \frac{\mathrm{d}\lambda}{\Delta\lambda}. \tag{7}$$

Then, assuming that the solar flux variation is small in $\Delta\lambda$, Eqs. (6) and (7) lead to

$$F^{\downarrow}_{\bar{\lambda},\mathrm{dir}}(\tau/\mu_0) \cong \mu_0 F_0(\lambda)(1 - A_{\bar{\lambda}}(\tau/\mu_0)). \tag{8}$$

Integrating Eq. (8) over the entire solar spectrum, the total flux $F^{\downarrow}_{\mathrm{dir}}(\tau/\mu_0)$ may be expressed as

$$F^{\downarrow}_{\mathrm{dir}}(\tau/\mu_0) = \int_0^\infty \mu_0 F_0(\lambda)(1 - A_{\bar{\lambda}}(\tau/\mu_0))\mathrm{d}\lambda. \tag{9}$$

Trivially, the radiation received at the TOA may be written as

$$\mu_0 F_0 = \int_0^\infty \mu_0 F_0(\lambda)\mathrm{d}\lambda. \tag{10}$$

Thus, dividing Eq. (9) by Eq. (10)

$$\frac{F_{\mathrm{dir}}^{\downarrow}(\tau/\mu_0)}{\mu_0 F_0} = \int_0^{\infty} W(\lambda)(1 - A_{\bar{\lambda}}(\tau/\mu_0))\mathrm{d}\lambda, \tag{11}$$

where $W(\lambda)$ is the ratio of the extraterrestrial energy in a band $\mathrm{d}\lambda$.

Defining the total absorption $A(\tau/\mu_0)$ as

$$A(\tau/\mu_0) = \int_0^{\infty} W(\lambda) A_{\bar{\lambda}}(\tau/\mu_0)\mathrm{d}\lambda, \tag{12}$$

Eq. (11) may be written as

$$\frac{F_{\mathrm{dir}}^{\downarrow}(\tau/\mu_0)}{\mu_0 F_0} = 1 - A(\tau/\mu_0). \tag{13}$$

Let us now consider the particular case in which the dependence of the optical thickness with the wavelength throughout the interval $\Delta\lambda$ can be neglected. In that case, Eq. (7) may be written as

$$A_{\bar{\lambda}}(\tau/\mu_0) = 1 - e^{-\tau_\lambda/\mu_0}. \tag{14}$$

Leading Eq. (9) to

$$\frac{F_{\mathrm{dir}}^{\downarrow}(\tau/\mu_0)}{\mu_0 F_0} = \int_0^{\infty} W(\lambda) e^{-\tau_\lambda/\mu_0}\mathrm{d}\lambda. \tag{15}$$

ACPD
14, 20231–20257, 2014

Therefore, from Eqs. (13) and (15), the total absorption can be isolated and computed as

$$A(\tau/\mu_0) = 1 - \int_0^{\infty} W(\lambda) e^{-\tau_\lambda/\mu_0} \mathrm{d}\lambda \tag{16}$$

In the particular case of the ozone, the optical thickness defined from the TOA to a level z may be expressed as

$$\tau_\lambda(z) = \int_z^{\infty} k_\lambda \rho q_{O_3} \mathrm{d}z, \tag{17}$$

where k_λ denotes the mass absorption cross section and ρ is the dry air density.

If a medium is homogeneous, the absorption coefficient becomes independent of the temperature and the pressure and Eq. (17) may be expressed by

$$\tau_\lambda(z) = k_\lambda \int_z^{\infty} \rho q_{O_3} \mathrm{d}z. \tag{18}$$

The atmosphere is not homogeneous and not all the shortwave schemes in the WRF-ARW model use this approach. As aforesaid in Sect. 2.1, only the New Goddard and the CAM parameterizations consider k_λ as a constant with height.

Extending the integral over the entire atmosphere and assuming the hydrostatic equilibrium given by Eq. (2), Eq. (18) may be written as

$$\tau_\lambda(p_s) = \frac{k_\lambda}{g} \int_0^{p_s} q_{O_3} \mathrm{d}p. \tag{19}$$

ACPD
14, 20231–20257, 2014

In virtue of Eq. (3), the optical thickness may be expressed as

$$\tau_\lambda(p_s) = \frac{k_\lambda}{g} TO_3. \tag{20}$$

Substituting Eq. (20) into Eq. (16), the total absorption may be written as

$$A(\tau/\mu_0) = 1 - \int_0^\infty W(\lambda) e^{-\frac{k_\lambda}{g\mu_0} TO_3} d\lambda. \tag{21}$$

The necessary information to compute the $A(\tau/\mu_0)$ in Eq. (21) are the TO_3, $W(\lambda)$, k_λ and μ_0. Information about the TO_3 can be obtained from Sect. 2.2. The $W(\lambda)$, k_λ are data available in the source code of each shortwave scheme (i.e. New Goddard and CAM). Finally, the cosine of the solar zenith angle μ_0 may be computed as a function of the latitude, the longitude, the hour and the day of the year.

From the expression 21, we can conclude that, given a fixed wavelength, there are two variables that may change the ozone absorption over the globe. On the one hand, the cosine of the solar angle increases the absorption as solar beams travel throughout a longer path when the Sun is near to the horizon than when is normal to the surface. On the other hand, the total ozone column increases or decreases the opacity of the atmosphere, absorbing more or less energy.

To avoid day/night problems throughout the zonal direction, all longitudes assume midday in local time (i.e. the minimum slant respect the normal in the optical thickness). In the meridional direction, those latitudes showing a solar zenith angle greater than 80° are considered as night (i.e. polar night).

Under these considerations, given a shortwave scheme, Eq. (21) is applied over each node of the grid for all months. To calculate the bias, the absorption is computed using as TO_3, the original and MSR datasets. For a given month m, let us assume $A_{sch}(i,j)(m)$ and $A_{MSR}(i,j)(m)$ the absorption result for the ozone dataset of the scheme and the MSR, respectively, for a node at i (west–east direction) and j (south–north direction). The bias of the parameterization $\mathrm{BIAS}_{ij}(m)$ may be defined as

$$\mathrm{BIAS}_{ij}(m) = A_{\mathrm{sch},ij}(m) - A_{\mathrm{MSR},ij}(m) \tag{22}$$

Note that this metric is not normalized but it has units of parts per unit due to total absorptions are normalized respect to the flux at the TOA.

3 Results

3.1 Part one: study of the simplifications assumed in the ozone profiles

In this section, ozone profiles provided with the WRF-ARW model are evaluated following the procedures described in Sect. 2.2. We first focus on detailing results for each dataset (i.e. RRTMG, G-NG-FLG and CAM) over the globe. After this, there is a general discussion of the spatial and temporal deviation patterns.

In the RRTMG scheme shown, in Fig. 1, the lowest deviations of the total ozone column are observed along the mid-latitudes of each hemisphere during the respective (i.e. Northern or Southern Hemisphere) winter and spring, lower in the Northern than in the Southern. The global minimum is reached in May, in Siberia (−8 %) and along Europe (−3 %). With the exception of the ozone hole, the largest departures in the total ozone column are observed along the tropics (+35 to +60 %) as a function of the month. An asymmetry with respect to the Equator line is observed, reaching the highest overestimation in the winter hemisphere due to the low ozone production. The global maximum is observed over Antarctica in September (+90 to +100 %) and October (+90 to +130 %).

The G-NG-FGL results, Fig. 1, show a strong difference between the tropics and the midlatitudes and high latitudes. The tropics show the best accuracy over the year with values between −10 and +2 % with a tendency to underestimate the total ozone column values. Seasonally, positive and negative departures are observed over the

ACPD
14, 20231–20257, 2014

summer and winter hemispheres, respectively. Mid-latitudes and high latitudes show a high seasonal variability due to the ozone profiles are limited to winter or summer (Table 1). The mid-latitude winter profile shows positive deviations over both hemispheres, larger in the Southern during the Southern Hemisphere fall (+35 to +50 %) and lower in the Northern Hemisphere during the Northern Hemisphere winter (−15 to −5 % over the eastern side of Asia, −10 to 0 % over the northern side of the United States and 0 to +30 % over the rest). In January a near-zero belt around the 60° N is observed, which expands southward during February and March. In contrast, the mid-latitude summer profile drifts from slightly negative departures during the spring to slightly positive deviations in summer. The Arctic winter profile shows positive deviations over both hemispheres. The greatest values in the Northern Hemisphere are observed in October (+70 to +80 % over Greenland and the Scandinavian Peninsula) while the largest deviations in the Southern Hemisphere are reached in September (+135 to +155 % over Antarctica). The Arctic summer profile shows different patterns in each hemisphere. In the Northern Hemisphere, negative deviations (−15 to −5 %) are observed during the spring drifting into positive departures in summer (+5 to +15 % in July, +10 to +20 % in August and +15 to +25 % in September) with near-zero values in June. The Southern Hemisphere shows positive departures during all the months reaching the maximum value in October over Antarctica (+95 to +105 %).

Finally, in the CAM case, Fig. 2, the latitudinal and seasonal variations are well emulated with departures between the −10 and the +10 % with a clear overestimation. The largest departures are a result of the lack of consideration of the longitudinal ozone variations in the datasets available to the shortwave radiation schemes. Departures between +20 and +25 % are reached over January and February in a defined region between Greenland and the Scandinavian Peninsula. Moreover, the east-west variations due to the ozone hole produce a high overestimated region (between +30 and +40 % with peaks above +45 %) around the Greenwich's meridian and a high underestimation region (−20 to −10 %) in the opposite side of Antarctica. In November and December,

ACPD
14, 20231–20257, 2014

an overestimated region (+15 to +20 %) is observed over the Mediterranean basin and over the Sahara.

Latitudinally and seasonally, the distribution of the departures shows a logical coherence with the quality of the ozone profiles available in each shortwave scheme. Thus, the ozone dataset in the CAM scheme shows the lowest deviations while the largest errors are observed in the RRTMG. Generally, the total ozone column is overestimated by all the analyzed schemes with the exception of some locations, especially, for the G-NG-FGL profiles. The largest departures are observed over Antarctica during the ending Southern Hemisphere winter and the near Southern Hemisphere spring due to the ozone hole is smoothed in all the ozone datasets.

Longitudinally, similar distribution patterns can be observed for all the shortwave schemes because all of them assume meridional averages in the ozone mixing ratio. Two zones may be discussed. Firstly, during the Northern Hemisphere fall and winter, it is observed an underestimated region between the north-eastern side of Asia and the north-western side of Canada as well as an overestimated region between Greenland and the Scandinavian Peninsula. This pattern reflects the quasi-stationary features of the upper-air circulation due to the sea–land distribution in the Northern Hemisphere as discussed in Dütsch (1974) or in Fusco and Salby (1999). Secondly, strong longitudinal gradients in the distribution of the errors are observed over Antarctica due to the ozone hole in September and October. In the other locations, the east-west distribution of the errors may be neglected.

3.2 Part two: an analysis of the uncertainties added to the computation of the direct solar radiation

As previously noted in Sect. 2.3, the errors in the determination of the ozone profiles are propagated in the shortwave radiation results. In this section, systematic biases introduced in the modeling of the direct solar radiation are discussed focusing on two schemes: New Goddard and CAM. First, a detailed description of the uncertainties over

ACPD
14, 20231–20257, 2014

the globe is shown. Then, a general view of those limitations and their implications is discussed.

In the New Goddard scheme, the bias in the total absorption with respect to the radiation at TOA ranges from −1.0 to +1.0 % reaching peaks near +2.0 % values close to the poles. The absorption is slightly underestimated in the tropics for the entire year. Mid-latitudes regions show overestimated values in winter, more homogeneous and higher in the Southern Hemisphere than in the Northern, ranging from +0 to +0.7 %. Near-zero values are observed over North America and Asia and extended over Europe in March. An exception of this winter pattern occurs over the eastern side of Asia where bias greater than −0.4 % is observed. During the spring, negative and near-zero departures in the bias are observed over both hemispheres, higher in the Northern (from −0.4 % in April to near-zero values in June) than in the Southern (from slightly negative in October to near-zero in December). In summer, the departures drift from near-zero biases during the early season to positive values at the end of the summer. As in the winter season, the bias is higher in the Southern Hemisphere. During the fall, the largest negative bias is observed over both hemispheres reaching the maximum during the first months.

The CAM scheme shows the lowest biases in the total absorption of the solar beam due to the ozone. The bias is clearly positive during the whole year with the exception of the northern side of the Pacific Ocean from October to March reaching deviations of −1.0 % in December over the Asian coast and, in some regions over Antarctica from August to October, reaching departures around the −0.5 %. Two positive maximum are observed, one over Arctic from January to March with peaks around +1.0 % and, the other over Antarctica from September to November reaching a bias of +0.5 %. Although this scheme has the highest latitudinal resolution, the largest deviations are observed throughout high-latitudes because the ozone profiles simplify the meridional variations produced by the seasonal ozone depletion occurred since winter until near spring (Southern and Northern Hemisphere).

ACPD
14, 20231–20257, 2014

The results from this part of the study are generally consistent with the ozone column deviation results shown in Figs. 1 (G-NG-FLG) and 2. Both schemes tend to overestimate the absorption with lower departures in the tropics than in the middle or high latitudes and a maximum over Antarctica during the early Southern Hemisphere spring. As opposed to the results in Sect. 3.1, the impact of these errors on the simulation of the shortwave irradiance at the surface is linked to the Sun's position. The highest ozone biases in the poles are masked by their coincidence with the polar night. However, the low solar elevation angles at high latitudes results in a higher sensitivity to the ozone datasets in these latitudes. These factors combine to produce the largest meridional gradients in the errors in the modeling of direct solar radiation in the high latitudes during the winter season of each hemisphere.

4 Conclusions

Two sets of conclusions can be derived from the results of the analysis presented in this paper. The first set is related to the quality of the ozone concentration datasets available to the WRF-ARW mesoscale model and the second set is associated with the impact of these deficiencies in representing the spatial and temporal variations of the ozone profiles on the performance of the shortwave radiation schemes available to WRF-ARW model users.

The key point is that the analysis indicates that the ozone profiles available in the WRF-ARW package are a poor representation of the ozone distribution over the planet during a typical year. These datasets assume zonal averages in the ozone mixing ratio and describe the anomalies in latitude and in time with a low resolution.

In general, the largest deviations are observed over the polar latitudes during the winter of each hemisphere due to the ozone depletion, greater in Antarctica than in Arctic.

All the WRF-ARW ozone datasets that were analyzed in this study exhibited similar longitudinal error patterns. The error patterns were more prominent in the Northern

ACPD
14, 20231–20257, 2014

Hemisphere due to the quasi-stationary features associated with the land–sea distribution that are not captured in the ozone profiles. As consequence, a systematic underestimation of the total ozone column is observed in a region between the east of Asia (i.e. eastern Russia) and the west of North America (i.e. Alaska and Western Canada) during the Southern Hemisphere winter and near spring. In contrast, a systematic overestimation occurs in a region defined between Greenland and the Scandinavian Peninsula during the Southern Hemisphere fall and near winter.

The RRTMG, with a single ozone profile for all the latitudes and seasons, is the shortwave scheme with the poorest ozone resolution and the largest departures in front of the climatology. Only the northern mid-latitudes show small deviations as consequence that was calibrated in that latitudes.

The ozone profiles used by the Goddard, New Goddard and the Fu–Liou–Gu consider five ozone profiles: tropical, mid-latitude (winter/summer) and Arctic (winter/summer) for both hemispheres. This discretization show better results in the Northern Hemisphere than in the Southern. The tropical profile shows a systematic underestimation of the ozone amount over any longitude, greater in the summer hemisphere, near-zero in the winter hemisphere and practically homogeneous during the equinoxes. This underestimation pattern is directly linked to the obliquity of the ecliptic and the available insolation which produce more ozone in summer than in winter. Positive departures are observed over the mid-latitudes in winter and in summer, better in the second for both hemispheres. Negative deviations are observed during spring while the worst results of the year are obtained during fall. A similar pattern is observed in the polar regions with greater differences between the northern and the southern as discussed at the beginning of this section.

Finally, the CAM shortwave parameterization shows the lowest departures in the total ozone column. This scheme, composed by 64 ozone profiles with a monthly temporal resolution, captures a great part of the ozone variations over the globe. The largest deviations are observed throughout the longitudes because of the zonal averages in

ACPD
14, 20231–20257, 2014

the profile datasets. The highest zonal gradients in the errors are observed over the poles during the winter season of each hemisphere.

The second set of conclusions address the impact of the deficiencies in the specification of the ozone distribution on the simulation of the shortwave radiation. A key point is that the impact of errors in the representation of the spatial and temporal distribution of ozone on the model's simulation of shortwave radiation is determined by multiple factors and is not a simple function of the errors in the ozone profiles. For example, the largest errors in the ozone profiles were determined to be in the Polar Regions during winter. However, the impact of these errors on the simulation of shortwave radiation are masked by the coincidence of these errors with the polar night. On the other hand, the low solar elevation angles at high latitudes result in a higher sensitivity of the shortwave radiation schemes to the ozone profiles in these latitudes. These factors combine to produce the largest meridional gradients in the errors in the simulations of shortwave radiation in the high latitudes during the winter season of each hemisphere.

The lowest biases in the absorption of the solar direct beam occur over the tropics (Fig. 3) with near-zero departures. In contrast, the largest biases are observed poleward during the winter of each hemisphere. Longitudinally, underestimated ozone region over the northern Pacific produces important biases in the absorption.

The CAM parameterization shows lower biases (−1 to 1 %) than the New Goddard scheme (−1 to 3 %) with the same spatial and temporal distribution found in the total ozone errors as expected.

As conclusion, the ozone profiles provided with the WRF-ARW package have significant limitations because of their simplified representation of spatial and temporal variability of ozone concentrations. Those limitations introduce systematic biases in the modeling of shortwave radiation at surface becoming as a relevant point due to the growing interest in solar energy applications.

In virtue of the conclusions presented in this paper, a future study of the daily variation in the deviations could be valuable for solar short-term forecasting, since

ACPD
14, 20231–20257, 2014

introduced biases could be corrected by using different statistical postprocessing approaches (e.g. Model Output Statistics, MOS).

Acknowledgements. The research leading to these results has received funding from the Departament d'Economia i Coneixement de la Generalitat de Catalunya in the frame of the Talent empresa programme (grant: 2010-TEM-49).

References

Brewer, A.: Evidence for a world circulation provided by the measurements of helium and water vapour distribution in the stratosphere, Q. J. Roy. Meteor. Soc., 75, 351–363, 1949. 20234

Briegleb, B. P.: Delta–Eddington approximation for solar radiation in the NCAR Community Climate Model, J. Geophys. Res., 97, 7603–7612, 1992. 20236

Chandrasekhar, S.: Radiative Transfer, Dover Publications, New York, 1960. 20241

Chipperfield, M. and Jones, R.: Relative influences of atmospheric chemistry and transport on Arctic ozone trends, Nature, 400, 551–554, doi:10.1038/22999, 1999. 20233

Chou, M.-D. and Suarez, M. J.: A Solar Radiation Parameterization for Atmospheric Studies, NASA Tech. Memo, NASA/GSFC, 104606, 40, 1999. 20234, 20235

Chou, M.-D., Suarez, M. J., Liang, X.-Z., and Yan, M. M.-H.: A thermal infrared radiation parameterization for atmospheric studies, NASA Tech. Memo, 104606, 56, available at: http://ntrs.nasa.gov/search.jsp?R=20010072848 (last access: 1 August 2014), 2001. 20234, 20235

Collins, W. D., Rasch, P. J., Boville, B. A., Hack, J. J., McCaa, J. R., Williamson, D. L., Kiehl, J. T., Briegleb, B., Bitz, C., Lin, S., Zhang, M., and Dai, Y.: Description of the NCAR Community Atmosphere Model (CAM 3.0), NCAR Tech. Note NCAR/TN-464+ STR, Boulder, Colorado, 2004. 20234, 20235

Dee, D. P., Uppala, S. M., Simmons, A. J., Berrisford, P., Poli, P., Kobayashi, S., Andrae, U., Balmaseda, M. A., Balsamo, G.,Bauer, P., Bechtold, P., Beljaars, A. C. M., Berg, L., Bidlot, J., Bormann, N., Delsol, C., Dragani, R., Fuentes, M., Geer, A. J., Haimberger, L., Healy, S. B., Hersbach, H., Hólm, E. V., Isaksen, L., Kållberg, P., Köhler, M., Matricardi, M.,McNally, A. P., Monge-Sanz, B. M., Morcrette, J.-J., Park, B.-K., Peubey, C., Rosnay, P., Tavolato, C., Thépaut, J.-N., and Vitart, F.: The ERA-Interim reanalysis: configuration and performance

ACPD
14, 20231–20257, 2014

Analysis of the ozone profile specifications in the WRF-ARW model

A. Montornès et al.

Title Page
Abstract | Introduction
Conclusions | References
Tables | Figures
◀| |▶
◀ ▶
Back | Close
Full Screen / Esc
Printer-friendly Version
Interactive Discussion

of the data assimilation system, Q. J. Roy. Meteor. Soc., 137, 553–597, doi:10.1002/qj.828, 2011. 20234

Dobson, G. M.: Origin and distribution of the polyatomic molecules in the atmosphere, Proc. R. Soc. Lon. Ser.-A, 236, 187–193, 1956. 20234

Dudhia, J.: Numerical study of convection observed during the winter monsoon experiment using a mesoscale two-dimensional model, J. Atmos. Sci., 46, 3077–3107, doi:10.1175/1520-0469(1989)046<3077:NSOCOD>2.0.CO;2, 1989. 20235

Dütsch, H.: The ozone distribution in the atmosphere, Can. J. Chem., 52, 1491–1504, 1974. 20247

Fusco, A. and Salby, M.: Interannual variations of total ozone and their relationship to variations of planetary wave activity, J. Climate, 12, 1619–1629, 1999. 20247

Gu, Y., Liou, K., Ou, S., and Fovell, R.: Cirrus cloud simulations using WRF with improved radiation parameterization and increased vertical resolution, J. Geophys. Res., 116, D06119, doi:10.1029/2010JD014574, 2011. 20236

Lacis, A. A. and Hansen, J.: A parameterization for the absorption of solar radiation in the Earth's atmosphere, J. Atmos. Sci., 31, 118–133, 1974. 20236

Liou, K. N.: An Introduction to Atmospheric Radiation, vol. 84, International Geophysics Series, Academic Press, New York, 1980. 20236, 20241

Mlawer, E. J., Taubman, S. J., Brown, P. D., Iacono, M. J., and Clough, S. A.: Radiative transfer for inhomogeneous atmospheres: RRTM, a validated correlated-*k* model for the longwave, J. Geophys. Res., 102, 16663–16682, 1997. 20236

NOAA: US Standard Atmosphere, 1976, Tech. rep., NOAA-S/T, U.S. Government Printing Office, Washington, D.C., 1976. 20238

Parrondo, M. C., Gil, M., Yela, M., Johnson, B. J., and Ochoa, H. A.: Antarctic ozone variability inside the polar vortex estimated from balloon measurements, Atmos. Chem. Phys., 14, 217–229, doi:10.5194/acp-14-217-2014, 2014. 20233

Ramanathan, V. and Dickinson, R. E.: The Role of Stratospheric Ozone in the Zonal and Seasonal Radiative Energy Balance of the Earth-Troposphere System, J. Atmos. Sci., 36, 1084–1104, 1979. 20233

van der A, R. J., Allaart, M. A. F., and Eskes, H. J.: Multi sensor reanalysis of total ozone, Atmos. Chem. Phys., 10, 11277–11294, doi:10.5194/acp-10-11277-2010, 2010. 20234, 20239

WMO: Atmospheric Ozone, Tech. Rep. 16, Global Ozone Research and Monitoring Project, Geneva, 1986. 20235

Table 1. Description of the ozone profiles in the shortwave schemes in the WRF-ARW model. Dudhia and GFDL schemes are not analyzed in this study for the reasons mentioned in the text.

Scheme	Profiles	Latitudes	Time	Levels	Location in code
Dudhia	None	–	–	–	–
Goddard	5	3	Summer/Winter	75	Subroutine gsfcswrad in module_ra_gsfcsw.f90
New Goddard	5	3	Summer/Winter	75	Subroutine goddardrad in module_ra_goddard.f90
GFDL	148	37	4 seasons	41	Subroutine o3int in module_ra_gfdl.f90
RRTMG	1	1	Annual	31	Subroutine o3data in module_ra_rrtmg_lw.f90
CAM	768	64	12 months	59	Auxiliary file ozone.formatted
FLG	5	3	Summer/Winter	75	Subroutine o3prof in module_ra_flg.f90

ACPD
14, 20231–20257, 2014

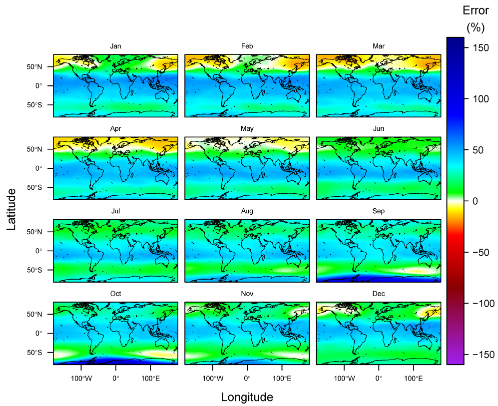

RRTMG

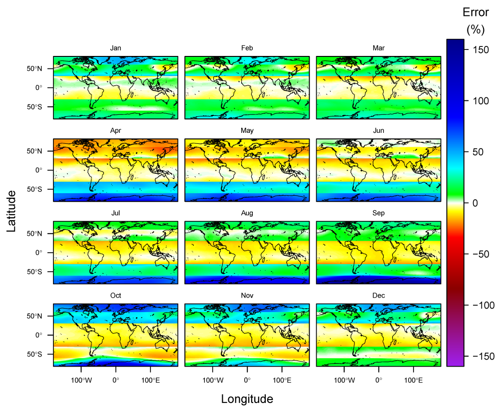

G-NG-FLG

Figure 1. Relative error in the total ozone column using the MSR monthly averages for the period (1979–2008) as baseline for RRTMG and G-NG-FLG.

ACPD
14, 20231–20257, 2014

Analysis of the ozone profile specifications in the WRF-ARW model

A. Montornès et al.

Title Page
Abstract | Introduction
Conclusions | References
Tables | Figures
◂I | I▸
◂ | ▸
Back | Close
Full Screen / Esc
Printer-friendly Version
Interactive Discussion

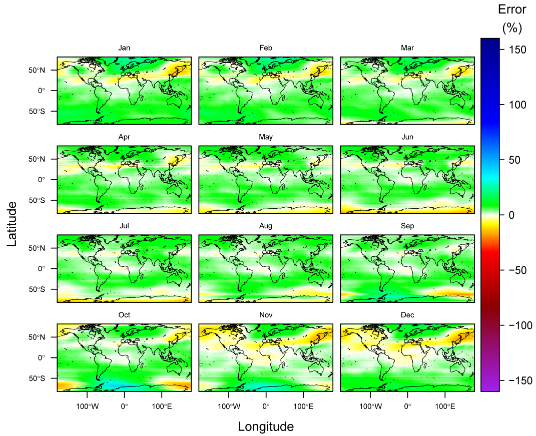

CAM

Figure 2. Relative error in the total ozone column using the MSR monthly averages for the period (1979–2008) as baseline for CAM.

ACPD
14, 20231–20257, 2014

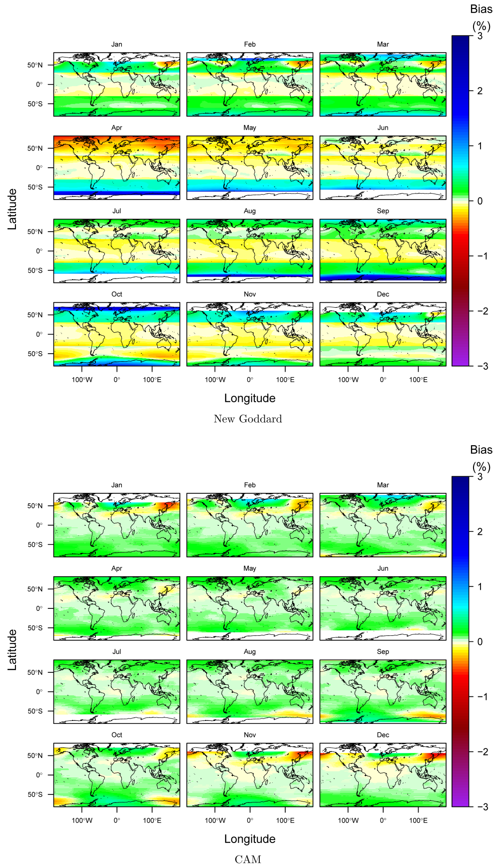

Figure 3. Bias in the ozone absorption using the MSR monthly averages for the period (1979–2008) as baseline for New Goddard and CAM.

ACPD
14, 20231–20257, 2014